







Measurements of the momentum-dependence of plasmonic excitations in matter around 1 Mbar using an X-ray free electron laser

T. R. Preston,^{1,a)}  K. Appel,¹  E. Brambrink,¹ B. Chen,¹ L. B. Fletcher,² C. Fortmann-Grote,¹  S. H. Glenzer,²  E. Granados,² S. Göde,¹ Z. Konôpková,¹ H. J. Lee,² H. Marquardt,^{3,4} E. E. McBride,^{1,2}  B. Nagler,² M. Nakatsutsumi,¹ P. Sperling,^{1,2} B. B. L. Witte,⁵ and U. Zastra¹ 

AFFILIATIONS

¹ European XFEL GmbH, Holzkoppel 4, 22869 Schenefeld, Germany

² SLAC National Accelerator Laboratory, 2575 Sand Hill Road, Menlo Park, California 94025, USA

³ Bayerisches Geoinstitut BGI, University of Bayreuth, 95440 Bayreuth, Germany

⁴ Department of Earth Sciences, University of Oxford, South Parks Road, Oxford OX1 3AN, United Kingdom

⁵ Institut für Physik, Universität Rostock, 18051 Rostock, Germany

a) thomas.preston@xfel.eu

ABSTRACT

We present measurements of the plasmon shift in shock-compressed matter as a function of momentum transfer beyond the Fermi wavevector using an X-ray Free Electron Laser. We eliminate the elastically scattered signal retaining only the inelastic plasmon signal. Our plasmon dispersion agrees with both the random phase approximation (RPA) and static Local Field Corrections (sLFC) for an electron gas at both zero and finite temperature. Further, we find the inclusion of electron-ion collisions through the Born-Mermin Approximation (BMA) to have no effect. Whilst we cannot distinguish between RPA and sLFC within our error bars, our data suggest that dynamic effects should be included for LFC and provide a route forward for higher resolution future measurements.

Matter with a high energy density, which is both warm and dense, is ubiquitous throughout the universe. This exotic state of matter is found in the cores of large planets,¹ the outer layers of stars,² and inertial confinement fusion reactions.^{3,4} However, diagnosing warm dense matter is challenging, as it exists between condensed matter theory and classical plasma physics, and cannot be simply described by either. Further, its high electron density renders it opaque to optical probes and its short lifespan mandates probing on ultra-short timescales. X-ray scattering techniques, encompassing X-ray diffraction and inelastic X-ray scattering, have been demonstrated as versatile and reliable diagnostic techniques.⁵ Inelastic scattering from collective electron modes yields information about thermodynamic properties (density and temperature),⁶ optical properties (dielectric function),^{7,8} and transport properties (electrical conductivity).⁹ The dielectric function is intimately related to the inelastic

scattering signal where energy is lost by the scattered photon by scattering from plasmon resonances. However, disentangling this signal from the brighter and broader elastic signal arising from the more numerous bound electrons requires narrow incoming X-ray bandwidths $\Delta E/E \sim 10^{-4}$ and sub-picosecond bright pulses for single-shot detection.¹⁰

The momentum-dependence of the plasmon resonance, or plasmon dispersion, is highly dependent on temperature and density.¹¹ A first approximation is often made using the steady-state Bohm-Gross dispersion as a function of electronic temperature and Debye length.¹² This amounts to a semi-classical approximate solution of the dispersion equation $\text{Re}[\epsilon(k, \omega(k))] = 0$ using the random phase approximation (RPA) dielectric function, ϵ . Corrections include quantum mechanical effects,⁹ electron-ion collisions,¹³ electron-electron correlations, and quantum degeneracy.¹⁴ These effects lead to differing dispersion relations,

in particular, at large momentum transfers above the Fermi wavevector.¹⁴ The ultimate future goal is to unequivocally discriminate between these modifications.¹⁵

It is with these caveats in mind that we present here measurements of the plasmon shift in shock-compressed matter over an extended wavevector range using an X-ray Free Electron Laser (FEL). Through measuring the pure elastic scattering signal from an insulator, contemporaneously with the upstream, incoming FEL signal, we are able to map the FEL signal to the predicted elastic scattering on a shot-by-shot basis, thus exposing the purely inelastically scattered signal. The cold, uncompressed, plasmon dispersion matches that measured experimentally.¹⁶ Simultaneous measurements of the diffraction signal provide information on the density of the shock-compressed aluminium. This measured density may be compared to the equation-of-state through one-dimensional radiation-hydrodynamic simulations in order to obtain the plasma temperature and peak pressure. We find a peak pressure over 1Mbar, and the density range is consistent between the diffraction data, compressed plasma frequency (which depends on electron density), and simulations. Calculations of the plasmon dispersion using both the random phase approximation (RPA) and static Local Field Corrections (sLFC) for an electronic gas at zero temperature with these found conditions match very well the measured plasmon shift at low wavevector, where these effects are indistinguishable, and at larger scattering angles (wavevectors). Including electron-ion collisions with the Born-Mermin Approximation (BMA) has no effect on the dispersion relations.

The experiment was performed at the Matter in Extreme Conditions (MEC)¹⁷ end-station of the Linac Coherent Light Source (LCLS). Aluminium foils of thickness 50 μm coated with 25 μm of parylene-N (plastic) were shock compressed to 1 Mbar using a temporally flat-top 6 ns pulse from the MEC Nd-Glass laser at a wavelength of $\lambda = 527 \text{ nm}$ with an energy of 6 J and a spot-size of diameter 200 μm in order to achieve uniform conditions. This shock-compressed Al was then probed at 6.5 ns, just before shock breakout of the back surface, by the LCLS FEL beam. The x-rays had a duration of 50 fs with a pulse energy of 1 mJ and a spot-size of diameter 20 μm and were incident at an angle of 30° to the target normal. The photon energy of the beam was tuned to $E = 7.2 \text{ keV}$ and LCLS was operated in the seeded mode providing a bandwidth $\Delta E/E$ of 10^{-4} .

Our primary diagnostic is the X-ray scattering signal which yields information on the collective electronic properties of the plasma. This is measured at two angles, 10° and 36° employing a 40 μm Highly Annealed Pyrolytic Graphite (HAPG) crystal in Von-Hamos geometry¹⁸ by placing the spectrometer azimuthally at 10° and then elevating it by 35° in polar angle. The acceptance angle of the crystal is $\pm 4^\circ$ due to the width of the crystal in the non-dispersive (azimuthal) direction. At higher scattering angles, the k -vector blurring introduced by the size of the crystal is reduced as the scattering vector is no longer aligned with the non-dispersive direction. These spectrometers combine high efficiency, required because of the low scattering cross-

section, with a moderate spectral resolution, in this study with a full width at half maximum (FWHM) around 7 eV.

First, the elastic scattering signal from 20 μm of parylene-N is recorded simultaneously with the upstream incident FEL spectrum for over 2000 shots for both spectrometer positions. The upstream spectrometer has a higher resolution,¹⁹ of order 0.3–0.5 eV, and can be used to distinguish the narrow incident x-rays against the self-amplified spontaneous emission (SASE) foot which was high because the accelerator was tuned to maximise the output energy. This enables us to map through a linear transformation matrix M the incident spectrum \mathbf{a} to the recorded elastically scattered spectrum $\mathbf{b} = M \cdot \mathbf{a}$ so that we can predict the shape of the elastic signal when Al is included. The transformation matrix is found simply from the vector product of the output and input spectra: $M = \mathbf{b} \otimes \mathbf{a}^{-1}$. Including Al in the target gives the average scattered signal, corrected for spatial jitter of the incident beam, as seen in Fig. 1(a) for both the cold (40 shots) and driven (29 shots) targets at 10°. Also shown is the average incident FEL spectrum for the cold shots (note that the spectrum is essentially identical for the driven

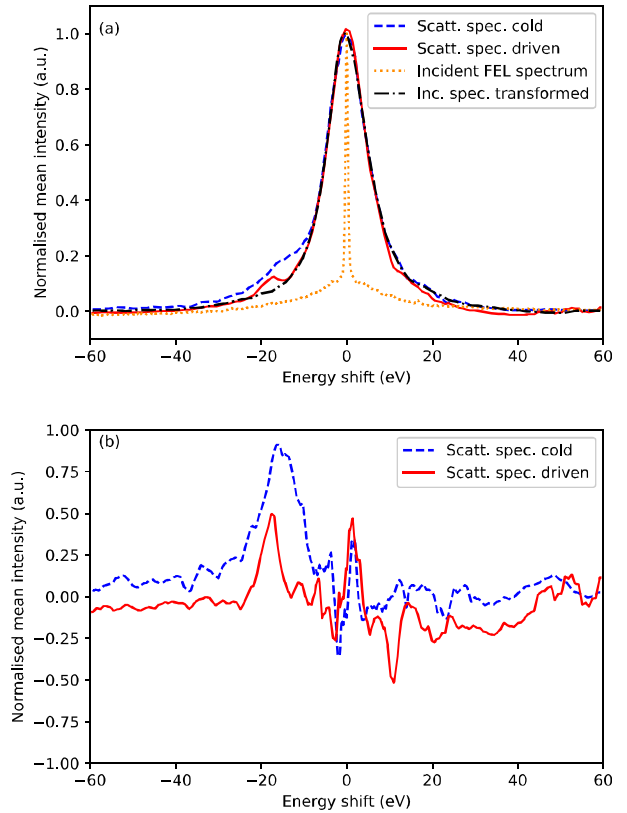


FIG. 1. (a) X-ray Thomson Scattering signal as a function of energy shift from the elastic peak for the cold (blue dashed) and driven aluminium (red solid) at a 10° scattering angle. Shown also is the incident FEL spectrum measured upstream (orange dotted) and the predicted elastic signal for this incident spectrum (black dot-dashed). (b) Scattering signals as in (a) but with the elastic signal subtracted yielding the cold (blue dashed) and driven (red solid) Al plasmon signal.

shots), and this spectrum transformed as described above to give the predicted elastic scattering signal (black). Subtracting this predicted elastic signal from the measured full signal reveals only the inelastic component in Fig. 1(b)—the electronic plasmon. The strong oscillations around the zero energy shift position are artefacts from subtraction (see supplementary material) and the correction of the spatial jitter arising from using a new target for every driven shot, which may sit differently in the focus. This has no effect on the position of the extracted plasmon. The method described above is also repeated at the higher spectrometer angle for 38 undriven and 34 driven shots and is shown in the supplementary material.

The short X-ray pulse gives a snapshot of the sample's conditions and is analysed through x-ray diffraction (XRD). The average diffraction pattern for all shots presented above is shown in Fig. 2 for the “Cold” (uncompressed) aluminium (78 shots) and the driven “Compressed” case (63 shots). Using the shift to higher angles (Q-shift) of the Bragg peaks (111), (200), and (220), we can extract a range of densities to which we compress the Al. All three agree and give a range of probed densities ρ of $1.29 < \rho/\rho_0 < 1.56$ as a ratio of the ambient density $\rho_0 = 2.7 \text{ g cm}^{-3}$. Further, the shock reproducibility can be analysed by considering the shock break-out time variability across all the shots using VISAR (Velocity Interferometer System for Any Reflector). The planarity of the shock is clear, and the break-out time is found to be consistent across all recorded shocks in the dataset at $7.90 \pm 0.36 \text{ ns}$.

Our other plasma conditions (temperature and pressure) are found from 1D radiation-hydrodynamic simulations using MULTI.²⁰ Given the laser temporal profile, the laser intensity is tuned to match the observed shock break-out time. The simulations indicate the presence of a release wave following the shock. In consequence, the x-ray beam probes the thermodynamic states of the shocked and partially released material following the

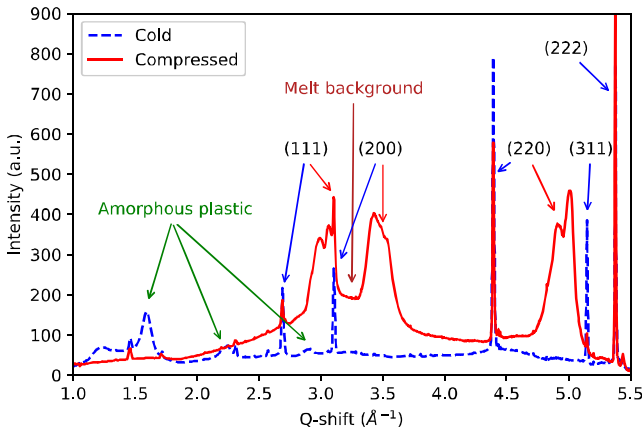


FIG. 2. X-ray diffraction pattern for aluminium both “Cold” (undriven, blue dashed) and “Compressed” (driven, red solid) as a function of momentum shift (Q-shift). Salient features of the pattern are identified such as the presence of amorphous plastic peaks, Bragg diffraction from Al both un- and compressed, and melt signature in the compressed case.

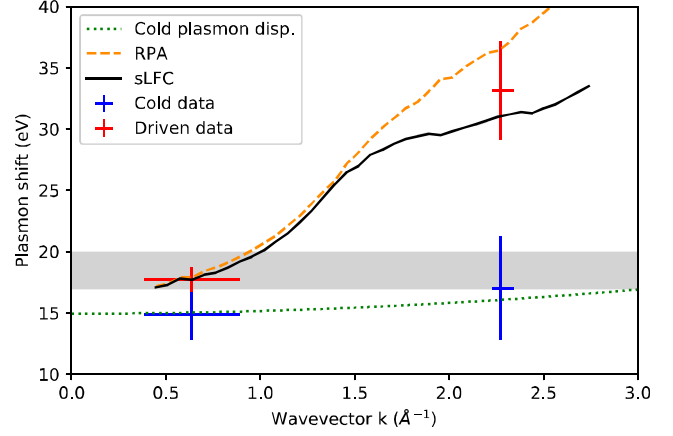


FIG. 3. Plasmon shift for aluminium both “Cold” (blue) and “Compressed” (red) as a function of wavevector (or momentum-transfer, k). Measurements are taken for $k = 0.6 \text{ \AA}^{-1}$ and $k = 2.3 \text{ \AA}^{-1}$. Also shown is the cold plasmon dispersion¹⁶ and the driven plasmon dispersion for RPA and for sLFC (at finite temperature).²⁴ The inclusion of electron-ion collisions via BMA has no effect on both of these plasmon dispersions. The grey band is the range of shifts expected at zero momentum-transfer for the density range measured from XRD.

isentrope from the initial shocked state as well as the unshocked material since probing was before the shock break out. The calculated density range in the compressed Al and the presence of an unshocked region agrees with the observed XRD (red solid curve, Fig. 2). The calculated temperature T in this compressed region is $0.25 < T(\text{eV}) < 0.37$, and the pressure P is $0.43 < P(\text{Mbar}) < 1.09$, indicating that under these conditions, we are just below the melt curve of Al,²¹ leading to partial melt on release. This again is corroborated by the XRD in Fig. 2, which shows a broad liquid feature from the Al melt underlying the Bragg peaks.

Our cold plasmon dispersion as a function of wavevector k matches measurements by Krane¹⁶ fitted to the empirical formula

$$\hbar\omega = \hbar\omega_p + \alpha \frac{(\hbar k)^2}{m_e}, \quad (1)$$

where \hbar is the reduced Planck constant, m_e the electronic mass, and the plasma frequency $\omega_p = \sqrt{n_e e^2 / m_e \epsilon_0}$, with e the electronic charge and ϵ_0 the permittivity of free-space. The fitting constant $\alpha = 0.46$ matches that found experimentally¹⁶ for $k > 0.5 \text{ \AA}^{-1}$ and is shown in Fig. 3.

Ordinarily, one would use an analytical form of the improved Bohm-Gross dispersion relation (IDR) to fit the plasmon dispersion which has the functional form¹³

$$\omega_{\text{IDR}}^2 = \omega_p^2 + \frac{3k_B T}{m_e} k^2 (1 + 0.088 n_e \Lambda_e^3) + \left(\frac{\hbar k^2}{2m_e} \right)^2, \quad (2)$$

where k_B is the Boltzmann constant and Λ_e is the thermal wavelength. However, this derivation assumes that the electron gas is weakly degenerate and the expansion of Fermi integrals used in its derivation requires that $y = n_e \Lambda_e / g_e < 5.5$, with g_e the electron spin degeneracy.²² Further, it is only valid for small momentum transfers k . For the plasmas considered here, $y \gg 100$; the degeneracy parameter of the plasma, which is the ratio of the

thermal energy to the Fermi energy,²² $\Theta = k_B T / E_F \ll 1$; and furthermore, the plasma is strongly coupled,²² $\Gamma \gg 1$. Consequently, our plasma is highly degenerate and requires more extensive modelling for the dispersion relation.

Fully calculated models of the compressed plasmon dispersion using the above conditions are then compared with the measured plasmon shift from Fig. 1(b) (and identically for the data at 36°). We choose conditions for our simulations which match the range of measured conditions above and agree with the 10° ($\rightarrow 0.6 \text{ \AA}^{-1}$) compressed plasmon shift. The best match is found for $\rho/\rho_0 \approx 1.3$, which corresponds to an electron density of $n_e = 2.3 \times 10^{23} \text{ cm}^{-3}$ and an electron temperature of $T = 0.3 \text{ eV}$. At this density, the Fermi wavevector $k_F = 1.9 \text{ \AA}^{-1}$, and furthermore, the scattering parameter $\alpha_s = \kappa_{TF}/k$, where $\kappa_{TF} = (m_e e^2 / \pi \epsilon_0 \hbar^2)^{1/2} (3n_e / \pi)^{1/6}$, the Thomas-Fermi inverse screening length¹⁵ for a degenerate plasma,²³ is calculated to be 3.6 at $k = 0.6 \text{ \AA}^{-1}$ and 0.9 at $k = 2.3 \text{ \AA}^{-1}$, implying that we are in the collective scattering regime at 10° and just outside it at 36°. Again, coinciding with the measured density from XRD, the 10° compressed plasmon shift matches the range of plasma frequencies with electron densities n_e determined from XRD shown as the grey-shaded band.

We compare the momentum-dependence of our compressed plasmon with two different models in Fig. 3. The first uses RPA which assumes that the electrons are distributed in nearly random positions and hence that their phases for different k average to zero.²⁵ The second augments this model with static Local Field Corrections (sLFC) which accounts for electronic interactions at high densities.¹⁴ Note that at very high densities, electron-electron collisions are however suppressed due to Pauli blocking (for $r_s \ll 1$).¹⁴ Both these models match very well with the measured dispersion at small wavevectors (scattering angle of 10°) but differ at higher momentum-transfers, where local field effects become important. However, due to the intrinsic resolution of the HAPG crystal employed by the spectrometer,¹⁸ as well as our diverse plasma conditions along the x-ray probe path, over which the plasmon position is averaged in each single shot, we are unable to resolve the peak position of the broad plasmon at higher scattering angles to better than $\pm 4 \text{ eV}$ and consequently are unable to distinguish between RPA and sLFC. Furthermore, neglecting finite temperature effects²⁶ has no effect on the dispersion since $\Theta = k_B T / E_F = 0.02$ and matches the shown curve for $T = 0.3 \text{ eV}$.²⁴ In addition to this, incorporating the Born-Mermin Approximation (BMA) which includes electron-ion collisions and, in the limit that $k \rightarrow 0$, converges to the Drude model for the dielectric function¹³ also has no effect on the dispersion curves. Nevertheless, our driven, high scattering-angle plasmon shift suggests that dynamic LFC should be included¹⁴ which is known to yield a smaller correction to the plasmon dispersion than its static counterpart.

In conclusion, we present measurements of the plasmon shift as a function of wavevector at two scattering angles: first at a low angle where the dispersion should not deviate strongly from the plasma frequency and second at a higher angle where deviations become apparent. We achieve this through subtracting the strong elastic scattering signal by characterising it shot-

by-shot and employing narrow bandwidth X-rays. Our shock-compressed plasmon is entirely consistent with the density measured from XRD, which itself closely follows that predicted from radiation-hydrodynamic simulations of the plasma. Given the density and temperature from these simulations, we construct plasmon dispersion models including different quantum-mechanical effects and compare these to our measured dispersion. We find both temperature effects^{24,26} and electron-ion collisions to be unimportant.¹³

Whilst plasmon measurements in this regime are not new, ours are made in more constrained conditions than previous work.¹⁵ We achieve this by using further complementary diagnostics including simultaneous shot-by-shot X-ray diffraction and VISAR measurements. Using these diagnostics, we are able to independently constrain our density and temperature without relying on fitting plasmon profiles as in Neumayer *et al.*¹⁵ and find results that are entirely consistent between all our diagnostics. For comparison, our measured density is found to within 10%, whereas Neumayer *et al.*¹⁵ infer a density from plasmon shifts within 18%. Previous work on plasmon measurements found agreement with LFC but not with RPA,¹⁵ however, their error bars on the measurements are smaller than ours and they find an even more depressed dispersion than with static LFC alone. Moreover, we concur that including Local Field Corrections is important.

Due to the resolution of the spectrometer crystal and the breadth of the compressed plasmon feature, we cannot distinguish between models including solely RPA and those which include static Local Field Corrections, but rather our work suggests that including dynamic LFC would better match our measured dispersion and may indeed be important. We assert that the method described in this letter is an effective method to measure plasmon dispersions in shock-compressed matter which would enjoy more profitable future success through the use of better statistics, higher repetition rate optical drive lasers, and higher energy-resolution spectrometers.

See supplementary material for the 36° scattering angle data, further details on the method to remove the elastic scattering, and 1D radiation-hydrodynamic simulations.

This work was performed at the Matter in Extreme Conditions (MEC) instrument of LCLS, supported by the DOE Office of Science, Fusion Energy Science under Contract No. SF00515. This work was further supported by Fusion Energy Sciences FWP100182. This work was also supported by LCLS, a National User Facility operated by Stanford University on behalf of the U.S. Department of Energy, Office of Basic Energy Sciences. E.E.M. was supported by the Volkswagen Foundation. C.F.G. acknowledges support from the European Cluster of Advanced Laser Light Sources (EUCALL) project which has received funding from the European Union's Horizon 2020 research and innovation programme under Grant Agreement No. 654220.

REFERENCES

- ¹T. Guillot, *Science* **286**, 72 (1999).
- ²F. J. Rogers and C. A. Iglesias, *Science* **263**, 50 (1994).

- ⁵J. D. Lindl, P. Amendt, R. L. Berger, S. G. Glendinning, S. H. Glenzer, S. W. Haan, R. L. Kauffman, O. L. Landen, and L. J. Suter, *Phys. Plasmas* **11**, 339 (2004).
- ⁶S. X. Hu, B. Militzer, V. N. Goncharov, and S. Skupsky, *Phys. Rev. Lett.* **104**, 235003 (2010).
- ⁷S. Glenzer and R. Redmer, *Rev. Mod. Phys.* **81**, 1625 (2009).
- ⁸H. J. Lee, P. Neumayer, J. Castor, T. Döppner, R. W. Falcone, C. Fortmann, B. A. Hammel, A. L. Kritcher, O. L. Landen, R. W. Lee, D. D. Meyerhofer, D. H. Munro, R. Redmer, S. P. Regan, S. Weber, and S. H. Glenzer, *Phys. Rev. Lett.* **102**, 115001 (2009).
- ⁹J. K. Cooper, S. Gul, F. M. Toma, L. Chen, Y.-S. Liu, J. Guo, J. W. Ager, J. Yano, and I. D. Sharp, *J. Phys. Chem. C* **119**, 2969 (2015).
- ¹⁰P. Sperling, S. Rosmej, R. Bredow, L. B. Fletcher, E. Galtier, E. J. Gamboa, H. J. Lee, H. Reinholz, G. Röpke, U. Zastrau, and S. H. Glenzer, *J. Phys. B: At., Mol. Opt. Phys.* **50**, 134002 (2017).
- ¹¹B. B. Witte, L. B. Fletcher, E. Galtier, E. Gamboa, H. J. Lee, U. Zastrau, R. Redmer, S. H. Glenzer, and P. Sperling, *Phys. Rev. Lett.* **118**, 1 (2017).
- ¹²L. B. Fletcher, E. Galtier, P. Heimann, H. J. Lee, B. Nagler, J. Welch, U. Zastrau, J. B. Hastings, and S. H. Glenzer, *J. Instrum.* **8**, C11014 (2013).
- ¹³L. B. Fletcher, H. J. Lee, T. Döppner, E. Galtier, B. Nagler, P. Heimann, C. Fortmann, S. LePape, T. Ma, M. Millot, A. Pak, D. Turnbull, D. A. Chapman, D. O. Gericke, J. Vorberger, T. White, G. Gregori, M. Wei, B. Barbrel, R. W. Falcone, C.-C. Kao, H. Nuhn, J. Welch, U. Zastrau, P. Neumayer, J. B. Hastings, and S. H. Glenzer, *Nat. Photonics* **9**, 274 (2015).
- ¹⁴D. Bohm and E. P. Gross, *Phys. Rev.* **75**, 1851 (1949).
- ¹⁵R. Thiele, T. Bornath, C. Fortmann, A. Höll, R. Redmer, H. Reinholz, G. Röpke, A. Wierling, S. H. Glenzer, and G. Gregori, *Phys. Rev. E: Stat., Nonlinear, Soft Matter Phys.* **78**, 1 (2008).
- ¹⁶C. Fortmann, A. Wierling, and G. Röpke, *Phys. Rev. E* **81**, 026405 (2010).
- ¹⁷P. Neumayer, C. Fortmann, T. Döppner, P. Davis, R. W. Falcone, A. L. Kritcher, O. L. Landen, H. J. Lee, R. W. Lee, C. Niemann, S. Le Pape, and S. H. Glenzer, *Phys. Rev. Lett.* **105**, 075003 (2010).
- ¹⁸K. J. Krane, *J. Phys. F: Met. Phys.* **8**, 2133 (1978).
- ¹⁹B. Nagler, B. Arnold, G. Bouchard, R. F. Boyce, R. M. Boyce, A. Callen, M. Campell, R. Curiel, E. Galtier, J. Garofoli, E. Granados, J. Hastings, G. Hays, P. Heimann, R. W. Lee, D. Milathianaki, L. Plummer, A. Schropp, A. Wallace, M. Welch, W. White, Z. Xing, J. Yin, J. Young, U. Zastrau, and H. J. Lee, *J. Synchrotron Radiat.* **22**, 520 (2015).
- ²⁰U. Zastrau, A. Woldegeorgis, E. Förster, R. Loetzsch, H. Marschner, and I. Uschmann, *J. Instrum.* **8**, P10006 (2013).
- ²¹D. Rich, D. Zhu, J. Turner, D. Zhang, B. Hill, and Y. Feng, *J. Synchrotron Radiat.* **23**, 3 (2016).
- ²²R. Ramis, R. Schmalz, and J. Meyer-Ter-Vehn, *Comput. Phys. Commun.* **49**, 475 (1988).
- ²³A. Hänström and P. Lazor, *J. Alloys Compd.* **305**, 209 (2000).
- ²⁴A. Höll, T. Bornath, L. Cao, T. Döppner, S. Düsterer, E. Förster, C. Fortmann, S. H. Glenzer, G. Gregori, T. Laarmann, K. H. Meiwes-Broer, A. Przystawik, P. Radcliffe, R. Redmer, H. Reinholz, G. Röpke, R. Thiele, J. Tiggesbäumker, S. Toleikis, N. X. Truong, T. Tschentscher, I. Uschmann, and U. Zastrau, *High Energy Density Phys.* **3**, 120 (2007).
- ²⁵G. Gregori, S. H. Glenzer, W. Rozmus, R. W. Lee, and O. L. Landen, *Phys. Rev. E: Stat. Phys., Plasmas, Fluids, Relat. Interdiscip. Top.* **67**, 10 (2003).
- ²⁶S. Ichimaru, S. Mitake, S. Tanaka, and X.-Z. Yan, *Phys. Rev. A* **32**, 1775 (1985).
- ²⁷D. Pines and D. Bohm, *Phys. Rev.* **85**, 338 (1952).
- ²⁸B. Farid, V. Heine, G. E. Engel, and I. J. Robertson, *Phys. Rev. B* **48**, 11602 (1993).